International Scholarly Research Network
ISRN Spectroscopy
Volume 2012, Article ID 706398, 8 pages
doi:10.5402/2012/706398

Research Article

Mn_3O_4 Nanoparticles: Synthesis, Characterization, and Dielectric Properties

Hassouna Dhaouadi,[1] Ouassim Ghodbane,[1] Faouzi Hosni,[2] and Fathi Touati[1]

[1] *Laboratoire des Matériaux Utiles, Institut National de Recherche et d'Analyse Physico-Chimique, Pôle Technologique de Sidi-Thabet, 2020 Tunis, Tunisia*
[2] *Unité de Radiotraitement, Centre National des Sciences et Technologies Nucléaires (CNSTN), Pôle Technologique de Sidi Thabet, 2020 Tunis, Tunisia*

Correspondence should be addressed to Hassouna Dhaouadi, dhaouadihassouna@yahoo.fr

Received 11 December 2011; Accepted 2 January 2012

Academic Editors: J. M. Saniger and M. Soylak

Mn_3O_4 nanoparticles were prepared by a simple chemical route using cetyltetramethylammonium bromide (CTAB) as a template agent. Mn_3O_4 nanocrystals present an octahedral shape, and their crystallite size varies between 20 and 80 nm. They were characterized by XRD, SEM, DTA/TG, and IR spectroscopy. XRD studies confirm the presence of a highly crystalline Mn_3O_4 phase. The Rietveld refinement of the X-ray diffraction data confirms that Mn_3O_4 nanoparticles crystallize in the tetragonal system with space group I41/amd. DTA/TG and XRD measurements demonstrate the phase transition toward a spinel structure between 25 and 700°C. The electrical conductivity increases between 80 and 300°C, suggesting a semiconducting behaviour of Mn_3O_4. Both dielectric dispersion (ε') and dielectric loss (ε'') were investigated from 80 and 300°C in the frequency range of 10 Hz–13 MHz. The dielectric properties showed typical dielectric dispersion based on the Maxwell-Wagner model.

1. Introduction

Metal oxide nanocrystals are widely applied in catalysis, energy storage, magnetic data storage, sensors, and ferrofluids [1–4]. Tetramanganese oxides (Mn_3O_4) are particularly used as main sources of ferrite materials [5] and applied in numerous industrial fields such as magnetic [6], electrochemical [7], and catalysis [8, 9]. The particle size and morphology may be controlled by using various methods including solvothermal/hydrothermal [10, 11], vapor phase growth [12], vacuum calcining precursors [13], thermal decomposition [14], ultrasonic, gamma, and microwave irradiation [15–17], and chemical liquid homogeneous precipitation [18]. Therefore, Mn_3O_4 compounds show distinct shapes including nanoparticles [19], nanorods [20], nanowires [21], and tetragonal particles [22].

The electrical and magnetic properties of numerous nanomaterials are completely different from those of their bulk counterparts. Changes in dielectric properties were attributed to changes in particle size, shape, and boundaries [23, 24]. The modified dielectric properties were used as capacitors, electronic memories, and optical filters. Materials exhibiting a giant dielectric constant were already reported elsewhere [25–27]. The high dielectric permittivity and the low loss factors over a wide frequency range are always of a great interest [28]. In a previous work, we synthesized Mn_3O_4 nanomaterials with lozenge morphology under hydrothermal treatment [29]. The temperature dependence of the conductivity between 25 and 220°C obeys the Arrhenius law with activation energy of 0.48 eV. However, the present work describes the preparation of Mn_3O_4 nanomaterials with octahedral shape at room temperature by using a precipitation method. The magnetic properties of the Mn_3O_4 nanocrystals are also studied by the electron paramagnetic resonance (EPR) technique. To the best of our knowledge, only a limited number of studies of the dielectric properties of nanostructured Mn_3O_4 were reported [30–32]. The scope of the present work is to study the dielectric properties of nanostructured Mn_3O_4 nanoparticles as a function of the frequency and the temperature.

2. Experimental Procedure

2.1. Sample Preparation. The synthesis of Mn_3O_4 nanoparticles was performed at room temperature, using the precipitation route [18]. 0.22 mol of $MnCl_2 \cdot 6H_2O$ (Aldrich) was added to 0.44 mol of NaOH (Fluka) aqueous solution. Then 1.37 mmol cetyltetramethylammonium bromide (CTAB) (Sigma) was dispersed and homogenized under slowly magnetic stirring during 24 hours. The precipitate was filtered and carefully washed with distilled water for several times. The resulting product was dried in the oven at 80°C for 24 hours.

The formation of Mn_3O_4 compound in the alkaline aqueous solution may be formulated by the following reactions:

$$Mn^{2+} + 2OH^- \longrightarrow Mn(OH)_2, \quad (1)$$

$$Mn(OH)_2 \longrightarrow MnO + H_2O, \quad (2)$$

$$3\,MnO + \frac{1}{2}\,O_2 \longrightarrow Mn_3O_4. \quad (3)$$

Manganese ions are firstly reduced in alkaline media to $Mn(OH)_2$ and then decomposed into MnO (see (2) and (3)). Finally, MnO is oxidized to Mn_3O_4 by the atmospheric oxygen.

2.2. Characterisation Techniques. X-ray powder diffraction (XRD) measurements were performed using a Panalytical XPERT PRO MPD diffractometer operating with Cu Kα radiation (λ = 0.15406 nm). Crystallographic data (lattice parameters, space group) were determined by using the Highscore software. The XRD pattern was analyzed by the Fullprof program [33] based on the Rietveld method [34] in order to calculate the cell parameters.

Infrared (IR) spectra were recorded in the wavenumber range of 4000–400 cm^{-1} with a "Nicolet 380 Spectrometer." The samples were dispersed in pure KBr pellets. Thermal analyses were performed by using the "SetaramSetsys 1750" operating from 25 to 800°C at a heating rate of 5°C·min^{-1} under air atmosphere. Scanning electron microscopy (SEM) images were obtained by a Zeiss Stereoscan 440 instrument. Conductivity measurements were carried out from 80 to 240°C with 5–20°C steps by checking the complex impedance spectroscopy with a Hewlett Packard 4129A impedance analyzer. The signal frequency ranged from 10 to 13 MHz.

3. Results and Discussion

3.1. Crystal Structure, Size, and Morphology. Figure 1 shows XRD patterns of as-prepared Mn_3O_4 nanoparticles. The diffraction peaks correspond to the tetragonal Mn_3O_4 single phase (JCPDS Card 01-080-0382). The Rietveld refinement procedure was performed for the investigation of the crystalline structure of as-prepared nanocrystallites. Figure 1 presents the experimental and calculated patterns together with the differential one, deduced from the Rietveld refinement. Mn_3O_4 X-ray data were refined in the tetragonal system (space group I41/amd). An excellent agreement between experimental and calculated patterns is obtained (χ^2 = 1.04). The refined cell parameters of Mn_3O_4 structure are a = 5.7671 (1) Å, c = 9.4521 (1) Å, and V = 314.3401 (1) Å^3. The structure was refined according to these parameters: $R_{wp}(\%)$ = 2.08, $R_{exp}(\%)$ = 2.13, $R_B(\%)$ = 1.13, and $R_F(\%)$ = 1.37.

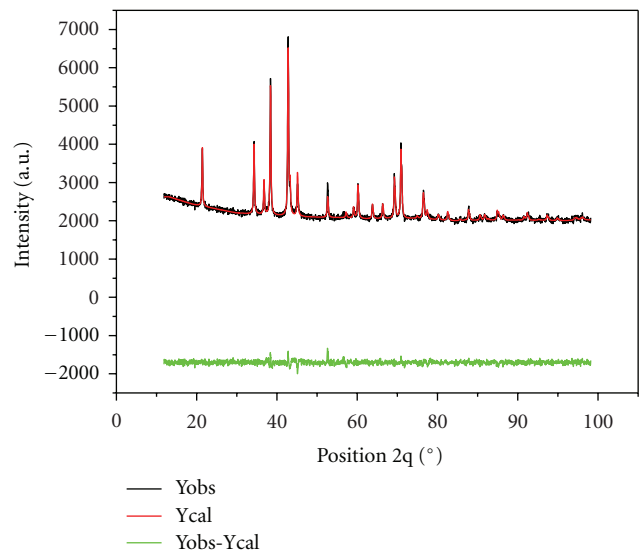

Figure 1: Rietveld refinement of the structure of Mn_3O_4 from XRD data.

The crystallite sizes were calculated from the major (211) diffraction peak using the Debye Scherrer approximation [35] and are about 50 nm. The morphology of Mn_3O_4 nanoparticles is shown in Figure 2. The formation of Mn_3O_4 nanoparticles is confirmed. Aggregated nanoparticles with octahedral shapes are observed, and their diameter varies between 20 and 80 nm. The SEM results of the Mn_3O_4 nanoparticles agree with the XRD data.

3.2. IR Absorption Spectroscopy. The IR absorption spectra of the pure CTAB and Mn_3O_4 nanopowders calcinated at different temperatures for 2 h are shown in Figure 3. The IR spectrum of as-prepared Mn_3O_4 nanoparticles without any thermal treatment displays three significant absorption bands in the range of 400–650 cm^{-1} (Figure 3(b)). The vibration frequency located at 629 cm^{-1} is characteristic of Mn–O stretching modes in tetrahedral sites, whereas the vibration frequency located at 510 cm^{-1} corresponds to the distortion vibration of Mn–O in an octahedral environment. The third vibration band, located at 410 cm^{-1}, can be attributed to the vibration of manganese species (Mn^{3+}–O) in the octahedral site of Mn_3O_4 [36–39]. Moreover, the broad band at 3436 cm^{-1} and the narrow one at 1646 cm^{-1} correspond to the O–H vibrating mode of the adsorbed water. The two intense adsorption bands located at 2920 and 2840 cm^{-1} are assigned to the symmetric and asymmetric stretching modes of the $-CH_2$ group of the CTAB surfactant bounded to the surface of Mn_3O_4, respectively. A comparison of the IR spectrum for pure CTAB (Figure 3(a))

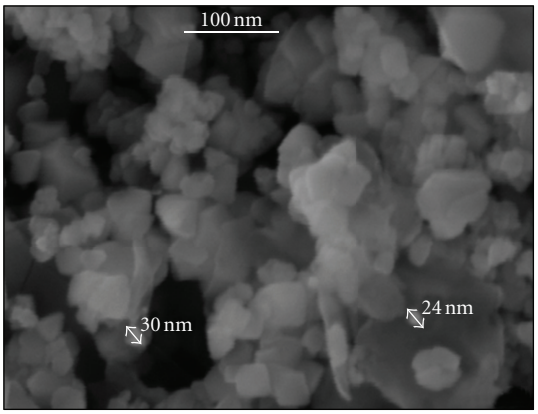

(a)

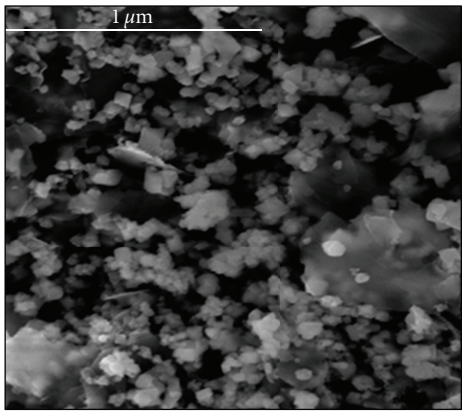

(b)

Figure 2: SEM images of Mn_3O_4 nanoparticles.

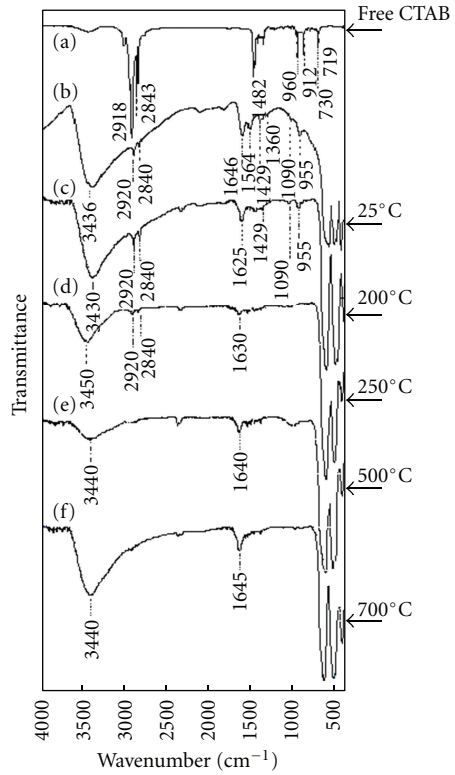

Figure 3: IR spectra of Mn_3O_4 nanoparticles calcined at different temperatures.

and the spectra relative to the Mn_3O_4 nanoparticles (Figures 3(b), 3(c), and 3(d)) shows invariant frequency positions at 2920, 2840 cm^{-1}, suggesting the absence of intermolecular interactions (C–H$\cdots$O) between oxygen atoms of Mn_3O_4 nanoparticles and the –CH_2 groups belonging to the CTAB surfactant. The difference between symmetric and asymmetric scissoring vibrations of $(CH_3)_3$–N^+ group of the pure CTAB (1482 cm^{-1}) and CTAB capped on the Mn_3O_4 nanoparticles surface (1429 cm^{-1}) reveals that CTAB adsorbed on the nanoparticle surface interacts strongly with oxygen atoms of Mn_3O_4 (Figure 3(b)). The single band located at 960 cm^{-1} on CTAB spectrum (Figure 3(a)) and the narrow one at 955 cm^{-1} (Figure 3(b)) for bounded CTAB may be assigned to the (C–N^+) stretching mode. The frequency shift may be caused by the interaction between $(CH_3)_3$–N^+ group and the oxidized metal surface [40]. This type of interaction was also observed between the polymer hydroxypropyl cellulose (HPC) used as capping agent and the silver metal surface [41].

During the heat treatment of Mn_3O_4, the progressive removal of the organic surfactant is well demonstrated by the IR spectra (Figure 3(b)–(f)) recorded at different temperatures. After two hours of thermal treatment at 500°C, vibration bands corresponding to the surfactant molecules were not observed on IR spectra, indicating that all organic groups were removed. During the heating process, a clear difference is observed in the IR spectra, in the range 700–400 cm^{-1}, corresponding of the stretching bands of Mn–O. This change in the position bands between 300 and 700°C can be related to the phase transformation of Mn_3O_4. This result is in a good agreement with X-ray diffraction data.

3.3. Thermal Analyses. In order to examine the thermal stability of Mn_3O_4 nanoparticles, thermal gravimetric (TG) and differential thermal analyses (DTA) were carried out between 25 and 800°C (Figure 4). In the temperature range of 25–250°C, the weight loss of 9.15% can be related to the release of weakly adsorbed water molecules and to the removal of the organic entities of CTAB surfactant. The broad exothermic peak at about 350°C, associated with the mass gain, is about 0.4% (Figure 4). As confirmed by earlier studies [42–44], this thermal event can be corroborated by the fact that Mn_30_4 (Mn_1^{+II}, Mn_2^{+III}) can be transformed into Mn_5O_8 (Mn_2^{+II}, Mn_3^{+IV}) in the temperature range of 300–450°C [45]. The new (Mn_5O_8) phase is formed according to the following reaction:

$$Mn_3O_4 + \frac{2}{5}O_2 \longrightarrow \frac{3}{5}\ Mn_5O_8. \tag{4}$$

Mn_5O_8 phase is isostructural with $Cd_2Mn_3O_8$ and crystallizes in the monoclinic system (C2/m) [46]. Mn_5O_8 was

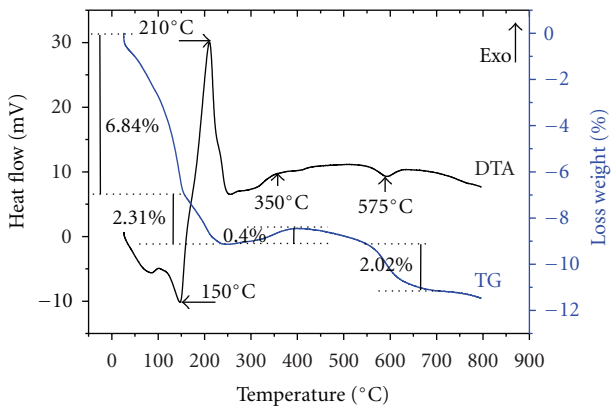

FIGURE 4: TG/DTA curves of Mn_3O_4 nanoparticles.

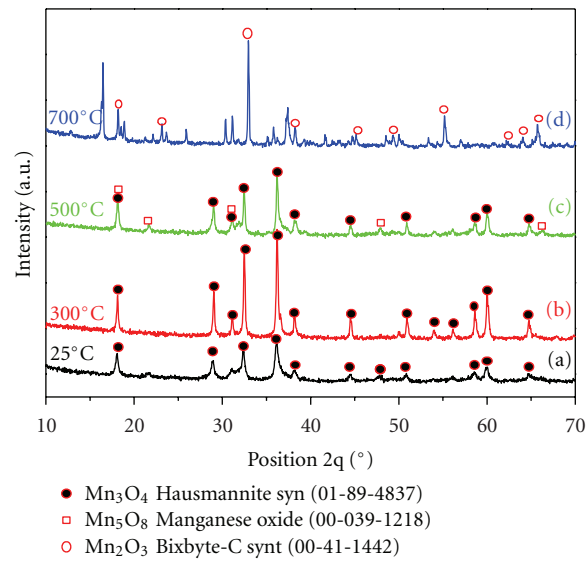

FIGURE 5: XRD patterns of Mn_3O_4 nanoparticles calcined at different temperatures.

observed during the decomposition of manganese oxalate [47] as well as in the transformation of hydrohausmannite into anhydrous hausmannite [46, 48]. The oxidation of Mn^{3+} to Mn^{4+} in the temperature range of 300–450°C leads to the crystallization of the Mn_5O_8 phase. After the exothermic peak at 350°C the mass remains relatively constant.

The endothermic event at 575°C, associated with the weight loss of 2.02% (calculated weight loss 1.98%), are related to the consequent release of oxygen due to the reduction of Mn_5O_8 to Mn_2O_3. The reaction scheme can be written as follows:

$$\frac{3}{5}Mn_5O_8 \longrightarrow \frac{3}{2}\,Mn_2O_3 + \frac{3}{20}O_2. \tag{5}$$

The weight loss is still constant at temperature higher than 700°C, indicating the completion of the thermal decomposition of the intermediate phase (Mn_5O_8) and the beginning of the crystallization of Mn_2O_3 as a new phase.

In order to give a plausible interpretation of the thermal phenomena, we also performed an investigation by X-ray diffraction analysis at different calcination temperatures for 2 h. Several samples of Mn_3O_4 nanoparticles were heated in electric oven (under air atmosphere) at different temperatures: 25, 300, 500, and 700°C, and they are immediately submitted to X-ray diffraction measurements (Figure 5). The X-ray diffraction of the product treated at 300°C is similar to that of the bare sample. This means that Mn_3O_4 nanoparticles are stable up to 300°C. In the temperature range of 25–300°C, XRD peaks gradually become sharper and higher, indicating an improved crystallinity. The X-ray diffraction spectrum at 500°C shows some additional peaks (Figure 5(c)). These diffraction peaks cannot be attributed to Mn_2O_3, and they are distinguishable from those of Mn_3O_4. They are observed at $2\theta = 21.741$, 31.916, 35.400, 39.250, 47.801, and 66.190° and indexed to (−201), (020), (−401), (002), (−421), and (−223) Bragg peaks, respectively. The corresponding phase is identified as Mn_5O_8 (JCPDS card no. 00-039-1218) [44]. It was already established that Mn_5O_8 is stable up to 550°C and transforms to Mn_2O_3 and Mn_3O_4 phases [49]. In the present case, after calcination at 700°C, the XRD spectrum (Figure 5(d)) shows that all diffraction peaks of Mn_5O_8 and Mn_3O_4 phases disappear. In the same way, a new phase Mn_2O_3 appears (JCPDS card no. 00-41-1442) with typical peaks at $2\theta = 19.02$, 23.28, 33.07, 35.87, 38.49, 55.44, and 65.92°. These peaks are indexed to (200), (211), (222), (321), (400), (440), and (622), respectively.

Paramagnetic properties of Mn_3O_4 nanoparticles calcined at different temperatures (25°C, 300°C, and 500°C) and cooled at room temperature were studied by the EPR technique (Figure 6). The paramagnetic properties were used in order to study the valence state changes of manganese element as a function of the temperature. Figures 6(a) and 6(b) indicate that the spectra mainly consist in one resonance line centered at $g_{\text{ref}} = 2.33$ that characterizes the unique paramagnetic center (Mn^{2+}) at each resonance feature. The broad EPR line seems to be originating from the electrostatic and dipolar interactions between the manganese ions with mixed valence states. Figure 6(c) shows two resonance peaks corresponding to the paramagnetic centers Mn^{2+} and Mn^{4+}, respectively. This indicates the presence of two Mn_5O_8 (Mn_2^{+II}, Mn_3^{+IV}) and Mn_3O_4 (Mn_1^{+II}, Mn_2^{+III}) phases around 500°C. Such a result is in good agreement with the XRD and thermal data and confirms the presence of two phases Mn_3O_4 and Mn_5O_8 around 500°C.

3.4. Conductivity Study. The temperature variation of the electrical conductivity between 80 and 300°C is represented in Figure 7 in the form of Ln (σT) versus 10^4/T. The electrical conductivity increases with increasing temperature. In the temperature range 80–140°C, the electrical conductivity approximately presents an Arrhenius-type behavior with an activation energy of $E_{a1} = 0.11$ eV. Around 140°C, a break in the curve is observed, accompanied by an increase of the activation energy ($E_{a2} = 0.56$ eV). This behaviour may be related to the removal of water molecules, residual ions, and organic surfactant capped on the surface of Mn_3O_4 particles. This probably affects the conductivity mechanism. It was reported elsewhere that the change in the slope does not

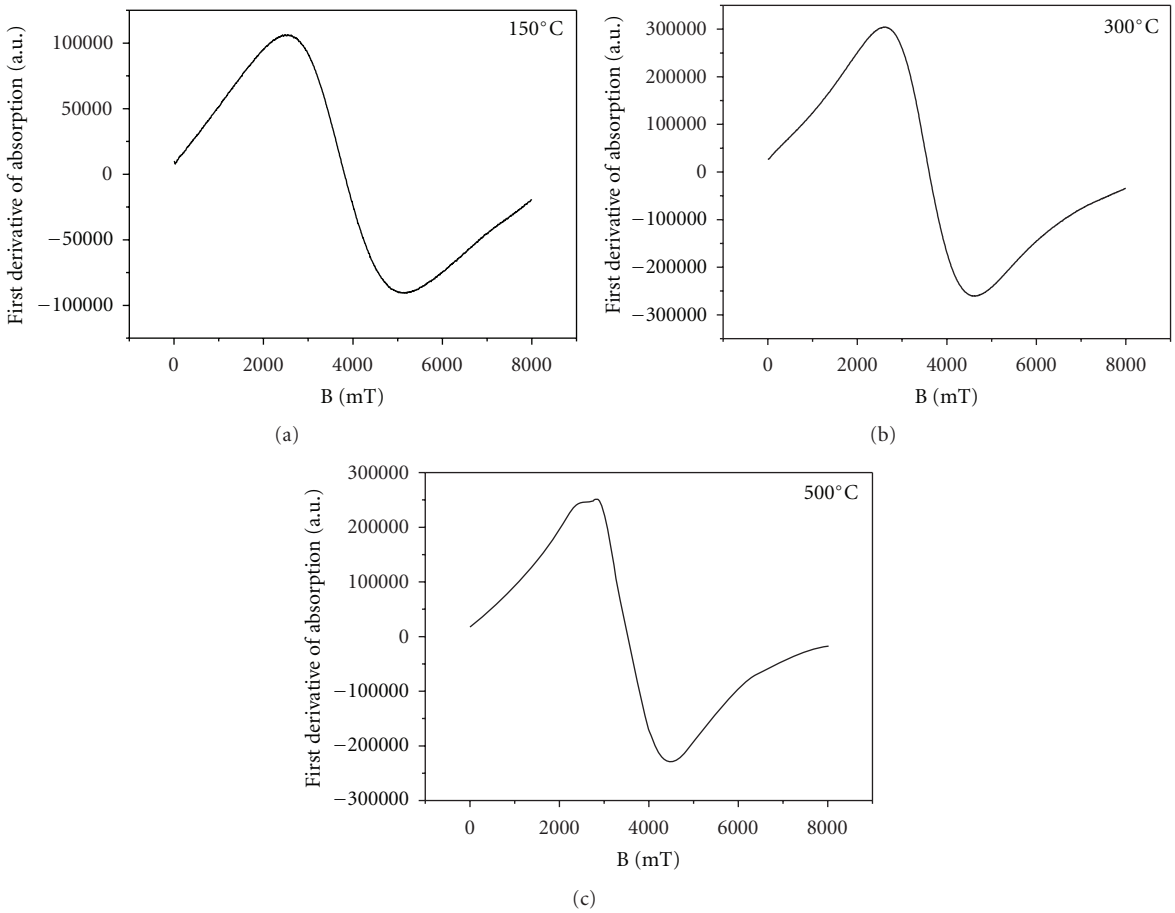

Figure 6: EPR spectra of Mn_3O_4 nanoparticles calcined at different temperatures.

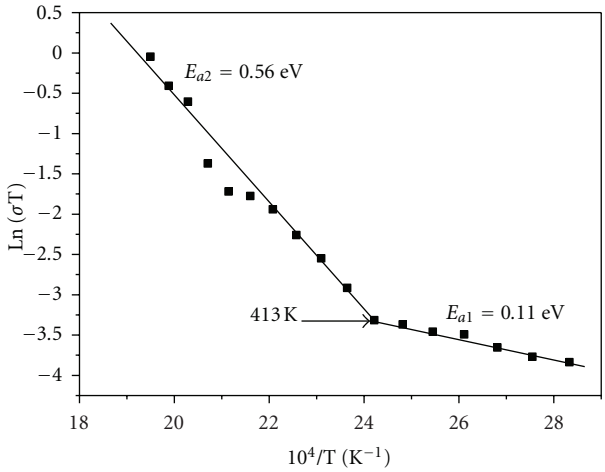

Figure 7: Arrhenius plot of the electrical conductivity for Mn_3O_4 nanoparticles.

occur for Mn_3O_4 nanoplatelet preliminarily heated at 300°C before being used in the conductivity study [29]. Larson and Arnott have measured the electrical conductivity of Mn_3O_4 bulk materials in the range 0–200°C. The obtained activation energy is 0.75 eV [50].

3.5. Dielectric Analysis. The complex dielectric permittivity is represented by $\varepsilon^* = \varepsilon' - i\varepsilon''$, where ε' is the real part of the dielectric permittivity that describes the stored energy, while ε'' is the imaginary part of dielectric permittivity related to the dissipation energy (or loss of energy) within the medium [51]. Figure 8(a) shows that the dielectric constant (ε') decreases continuously at lower frequencies and remains constant at higher frequencies giving rise to a plateau. The monotonous decrease in the value of dielectric constant on increasing frequency may be attributed to a combined contribution due to electronic, ionic, and interfacial polarization at low frequencies [52]. The observed dielectric dispersion at low frequencies can be explained on the basis of the Maxwell-Wagner theory of interfacial polarization [53]. According to the Maxwell-Wagner model, the dielectric structure of ferrites consists in two layers. The first layer represents a large number of grains that act as conducting layer at higher frequencies and the other layer consists in grain boundaries that act as highly resistive medium at lower frequencies. Similar results were observed for ferrite nanoparticles ($Mn_{0.2}Ni_{0.8}Fe_2O_4$) [54] as well as in bulk $SrNb_2O_6$ material [55]. At low frequencies, the polarization process in Mn_3O_4 nanoparticles is explained as a local displacement of electrons by hopping mechanism between Mn^{2+} and Mn^{3+} and an orientation of electric

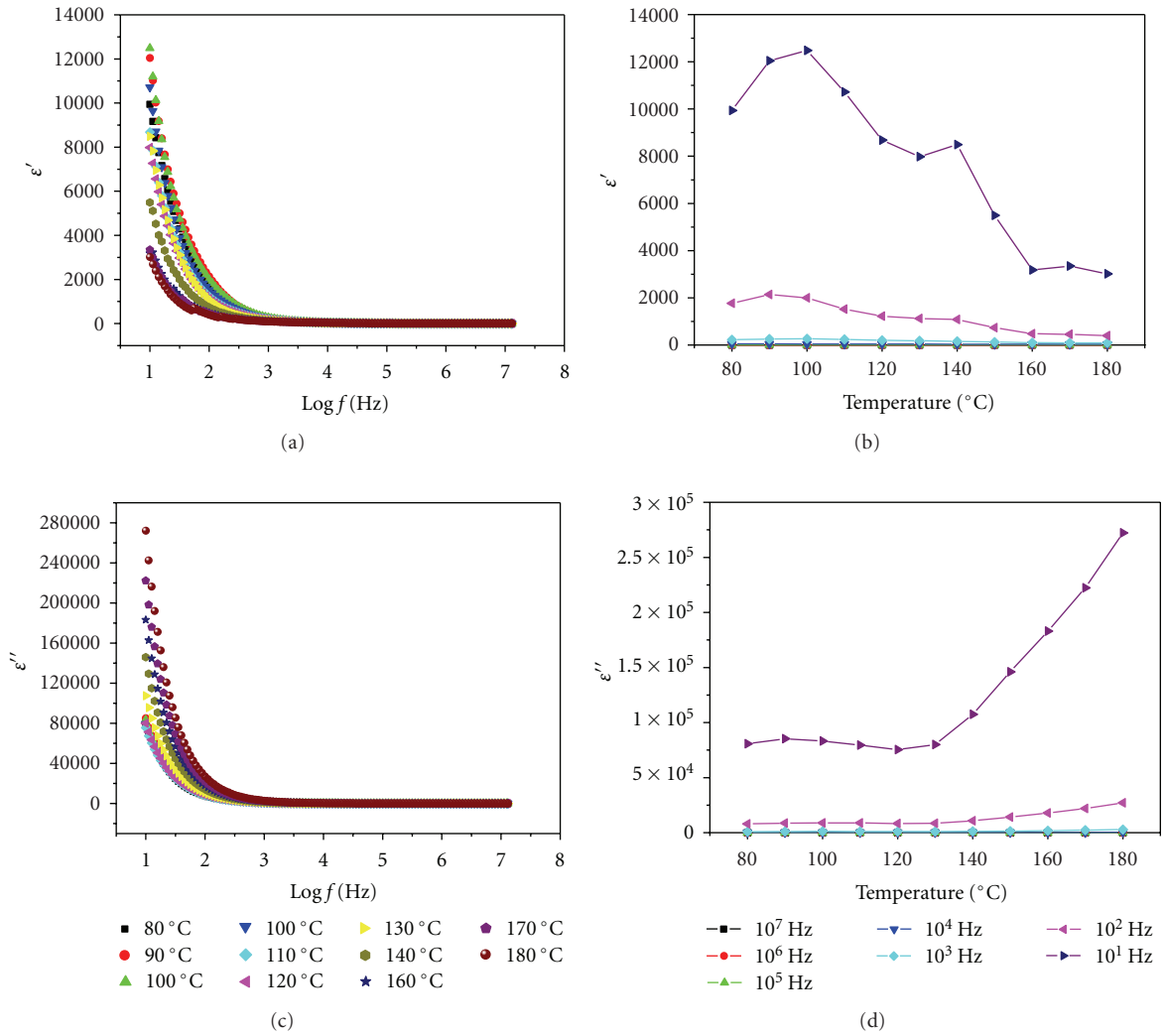

FIGURE 8: (a) Variation of dielectric constant ε' versus frequency at different temperatures for Mn_3O_4 nanoparticles. (b) Variation of dielectric constant (ε') versus temperature at different frequencies for Mn_3O_4 nanoparticles. (c) Variation of dielectric constant (ε'') versus frequency at different temperatures for Mn_3O_4 nanoparticles. (d) Variation of dielectric constant ε'' versus temperature at different frequencies for Mn_3O_4 nanoparticles.

dipole in the direction of the applied field. With increasing the frequency, electric dipoles, and the Mn^{2+}/Mn^{3+} electron transfer, the net displacement of charge in one direction decreases and then the dielectric constant decreases. The high dielectric values of the Mn_3O_4 nanoparticles are observed for other compounds such as ZnO nanotubes [56] and $Mn_{0.2}Ni_{0.8}Fe_2O_4$ nanoparticles [54] and for the bulk Mn-Mg spinel ferrite [57]. The large value of dielectric constant is due to the fact that Mn_3O_4 acts as a nanodipole under electric fields. The small-size particles involve large number of particles per unit volume resulting in an increase of the dipole moment per unit volume and the high dielectric constant.

The temperature dependence of dielectric permittivity (ε') at selected frequencies is represented in Figure 8(b). The dielectric permittivity increases gradually with the temperature until reaching a maximum value of T_{max}. On the other hand, relaxor ferroelectrics show a broad peak for the permittivity variation with the temperature at large frequency dispersion [58]. In the present case, a broad peak was observed in the temperature range of 90–120°C at low frequencies (Figure 8(b)). Other compounds show relaxor dielectric response such as $CrTiNbO_6$ [59] and $FeTiNbO_6$ [59]. The relatively insignificant variation of dielectric permittivity with the temperature observed at higher frequencies is attributed to atomic and electronic polarizations.

The imaginary part of the dielectric permittivity ε'' shows higher values that decrease rapidly with the frequency and increase as the temperature rises (Figure 8(c)). For nanometer-sized particles, the contribution of the interfacial loss and the loss from electrical conductivity is dominant at lower frequencies, but at high frequencies these losses are negligible. This may explain the decrease in dielectric constant (ε'') observed at high frequencies. The large value of the dielectric constant ε'' at lower frequency is due to the

predominance of Mn^{2+} ions, oxygen vacancies, and grain boundary defects [60, 61]. Figure 8(d) indicates that the imaginary part ε'' is fluctuating and increasing as a function of the temperature at higher frequencies. This suggests that the temperature dependency of the imaginary part is strongly dependent on the frequency range.

4. Conclusion

Mn_3O_4 nanoparticles were successfully prepared by using the precipitation method at room temperature in the presence of CTAB, as a template agent. X-ray structural analyses confirmed that Mn_3O_4 nanoparticles crystallize in the tetragonal system. From XRD and SEM results, Mn_3O_4 nanoparticles exhibit a crystallite size between 20 and 80 nm. XRD and DTA/TG analyses show the apparition of the metastable Mn_5O_8 phase at about 350°C. The paramagnetic properties of Mn_3O_4 samples were studied by the EPR technique in order to study the valence state changes with the temperature and to confirm the presence of the metastable Mn_5O_8 phase around 350°C. Dielectric measurement results show that ε' and ε'' decrease as the frequency increases. The dielectric dispersion ε' and the dielectric absorption ε'' of Mn_3O_4 nanoparticles are found to be slightly temperature dependent at higher frequency. These results indicate that the dielectric properties showed a usual dielectric dispersion explained on the basis of the Maxwell-Wagner model.

References

[1] A. J. Zarur and J. V. Ying, "Reverse microemulsion synthesis of nanostructured complex oxides for catalytic combustion," *Nature*, vol. 403, no. 6765, pp. 65–67, 2000.

[2] S. A. Majetich and Y. Jin, "Magnetization directions of individual nanoparticles," *Science*, vol. 284, no. 5413, pp. 470–473, 1999.

[3] C. Nayral, E. Viala, P. Fau et al., "Synthesis of tin and tin oxide nanoparticles of low size dispersity for application in gas sensing," *Chemistry. A European Journal*, vol. 6, no. 22, pp. 4082–4090, 2000.

[4] K. Raj and R. Moskowits, "Commercial applications of Ferro fluids," *Journal of Magnetism and Magnetic Materials*, vol. 685, p. 233, 1990.

[5] G. R. Mohan, D. Ravinder, A. V. Ramana Reddy, and B. S. Boyanov, "Dielectric properties of polycrystalline mixed nickel-zinc ferrites," *Materials Letters*, vol. 40, no. 1, pp. 39–45, 1999.

[6] A. Buckelew, J. R. Galán-Mascarós, and K. R. Dunbar, "Facile conversion of the face-centered cubic prussian-blue material $K_2[Mn_2(CN)_6]$ into the spinel oxide Mn_3O_4 at the solid/water interface," *Advanced Materials*, vol. 14, no. 22, pp. 1646–1648, 2002.

[7] S. T. Myung, S. Komaba, and N. Kumagai, "Hydrothermal synthesis and electrochemical behavior of orthorhombic $LiMnO_2$," *Electrochimica Acta*, vol. 47, no. 20, pp. 3287–3295, 2002.

[8] E. J. Grootendorst, Y. Verbeek, and V. Ponec, "The role of the mars and van krevelen mechanism in the selective oxidation of nitrosobenzene and the deoxygenation of nitrobenzene on oxidic catalysts," *Journal of Catalysis*, vol. 157, no. 2, pp. 706–712, 1995.

[9] E. R. Stobbe, B. A. De Boer, and J. W. Geus, "The reduction and oxidation behaviour of manganese oxides," *Catalysis Today*, vol. 47, no. 1–4, pp. 161–167, 1999.

[10] Y. C. Zhang, T. Qiao, and X. Ya Hu, "Preparation of Mn_3O_4 nanocrystallites by low-temperature solvothermal treatment of γ-MnOOH nanowires," *Journal of Solid State Chemistry*, vol. 177, no. 11, pp. 4093–4097, 2004.

[11] W. Zhang, Z. Yang, Y. Liu, S. Tang, X. Han, and M. Chen, "Controlled synthesis of Mn_3O_4 nanocrystallites and MnOOH nanorods by a solvothermal method," *Journal of Crystal Growth*, vol. 263, no. 1-4, pp. 394–399, 2004.

[12] Y. Q. Chang, D. P. Yu, Y. Long, J. Xu, X. H. Luo, and R. C. Ye, "Large-scale fabrication of single-crystalline Mn_3O_4 nanowires via vapor phase growth," *Journal of Crystal Growth*, vol. 279, no. 1-2, pp. 88–92, 2005.

[13] J. Du, Y. Gao, L. Chai, G. Zou, Y. Li, and Y. Qian, "Hausmannite Mn_3O_4 nanorods: synthesis, characterization and magnetic properties," *Nanotechnology*, vol. 17, no. 19, article no. 024, pp. 4923–4928, 2006.

[14] M. Salavati-Niasari, F. Davar, and M. Mazaheri, "Synthesis of Mn_3O_4 nanoparticles by thermal decomposition of a [bis(salicylidiminato)manganese(II)] complex," *Polyhedron*, vol. 27, no. 17, pp. 3467–3471, 2008.

[15] I. K. Gopalakrishnan, N. Bagkar, R. Ganguly, and S. K. Kulshreshtha, "Synthesis of superparamagnetic Mn_3O_4 nanocrystallites by ultrasonic irradiation," *Journal of Crystal Growth*, vol. 280, no. 3-4, pp. 436–441, 2005.

[16] Y. Hu, J. Chen, X. Xue, and T. Li, "Synthesis of monodispersed single-crystal compass-shaped Mn_3O_4 via gamma-ray irradiation," *Materials Letters*, vol. 60, no. 3, pp. 383–385, 2006.

[17] S. K. Apte, S. D. Naik, R. S. Sonawane et al., "Nanosize Mn_3O_4 (Hausmannite) by microwave irradiation method," *Materials Research Bulletin*, vol. 41, no. 3, pp. 647–654, 2006.

[18] Z. W. Chen, J. K. L. Lai, and C. H. Shek, "Nucleation site and mechanism leading to growth of bulk-quantity Mn_3O_4 nanorods," *Applied Physics Letters*, vol. 86, no. 18, Article ID 181911, pp. 1–3, 2005.

[19] A. Vázquez-Olmos, R. Redón, G. Rodríguez-Gattorno et al., "One-step synthesis of Mn_3O_4 nanoparticles: structural and magnetic study," *Journal of Colloid and Interface Science*, vol. 291, no. 1, pp. 175–180, 2005.

[20] Z. H. Wang, D. Y. Geng, Y. J. Zhang, and Z. D. Zhang, "Morphology, structure and magnetic properties of single-crystal Mn_3O_4 nanorods," *Journal of Crystal Growth*, vol. 310, no. 18, pp. 4148–4151, 2008.

[21] C. Du, J. Yun, R. K. Dumas et al., "Three-dimensionally intercrossing Mn_3O_4 nanowires," *Acta Materialia*, vol. 56, no. 14, pp. 3516–3522, 2008.

[22] M. Anilkumar and V. Ravi, "Synthesis of nanocrystalline Mn_3O_4 at 100°C," *Materials Research Bulletin*, vol. 40, no. 4, pp. 605–609, 2005.

[23] E. Veena Gopalan, K. A. Malini, S. Saravanan, D. Sakthi Kumar, Y. Yoshida, and M. R. Anantharaman, "Evidence for polaron conduction in nanostructured manganese ferrite," *Journal of Physics D*, vol. 41, no. 18, Article ID 185005, 2008.

[24] S. D. Shenoy, P. A. Joy, and M. R. Anantharaman, "Effect of mechanical milling on the structural, magnetic and dielectric properties of coprecipitated ultrafine zinc ferrite," *Journal of Magnetism and Magnetic Materials*, vol. 269, no. 2, pp. 217–226, 2004.

[25] M. A. Subramanian, D. Li, N. Duan, B. A. Reisner, and A. W. Sleight, "High dielectric constant in $ACu_3Ti_4O_{12}$ and $ACu_3Ti_3FeO_{12}$ phases," *Journal of Solid State Chemistry*, vol. 151, no. 2, pp. 323–325, 2000.

[26] A. P. Ramirez, M. A. Subramanian, M. Gardel et al., "Giant dielectric constant response in a copper-titanate," *Solid State Communications*, vol. 115, no. 5, pp. 217–220, 2000.

[27] P. Jha, S. Rai, K. V. Ramanujachary, S. E. Lofland, and A. K. Ganguli, "$(La_{0.4}Ba_{0.4}Ca_{0.2})(Mn_{0.4}Ti_{0.6})O_3$: a new titanomanganate with a high dielectric constant and antiferromagnetic interactions," *Journal of Solid State Chemistry*, vol. 177, no. 8, pp. 2881–2888, 2004.

[28] B. V. Prasad, G. Narsinga Rao, J. W. Chen, and D. Suresh Babu, "Abnormal high dielectric constant in $SmFeO_3$ semiconductor ceramics," *Materials Research Bulletin*, vol. 46, no. 10, pp. 1670–1673, 2011.

[29] H. Dhaouadi, A. Madani, and F. Touati, "Synthesis and spectroscopic investigations of Mn_3O_4 nanoparticles," *Materials Letters*, vol. 64, no. 21, pp. 2395–2398, 2010.

[30] D. Yan, S. Cheng, R. F. Zhuo et al., "Nanoparticles and 3D sponge-like porous networks of manganese oxides and their microwave absorption properties," *Nanotechnology*, vol. 20, no. 10, Article ID 105706, 2009.

[31] K. Usha and C. K. Mahadevan, "Structure, morphology and electrical properties of Mn_3O_4 nanocrystals," *Archives of Physics Research*, vol. 2, p. 75, 2011.

[32] E. Karaoğlu, H. Deligöz, H. Sözeri, A. Baykal, and M. S. Toprak, "Hydrothermal Synthesis and Characterization of PEG-Mn_3O_4 Nanocomposite," *Nano-Micro Letters*, vol. 3, p. 25, 2011.

[33] C. Rodriguez, "Recent advances in magnetic structure determination by neutron powder diffraction," *Physica B*, vol. 192, no. 1-2, pp. 55–69, 1993.

[34] H. M. Rietveld, "Line profiles of neutron powder-diffraction peaks for structure refinement," *Acta Crystallographica*, vol. 22, p. 151, 1967.

[35] H. P. Klug and L. E. Alexander, *X-ray Diffraction Procedures for Polycrystalline and Amorphous Materials*, chapter 9, Wiley, New York, NY, USA, 1st edition, 1954.

[36] M. Ishii, M. Nakahira, and T. Yamanaka, "Infrared absorption spectra and cation distributions in $(Mn, Fe)_3O_4$," *Solid State Communications*, vol. 11, no. 1, pp. 209–212, 1972.

[37] W. Z. Wang, C. K. Xu, G. H. Wang, Y. K. Liu, and C. L. Zheng, "Preparation of smooth single-crystal Mn_3O_4 nanowires," *Advanced Materials*, vol. 14, no. 11, pp. 837–840, 2002.

[38] N. Gupta, A. Verma, S. C. Kashyap, and D. C. Dube, "Microstructural, dielectric and magnetic behavior of spin-deposited nanocrystalline nickel-zinc ferrite thin films for microwave applications," *Journal of Magnetism and Magnetic Materials*, vol. 308, no. 1, pp. 137–142, 2007.

[39] S. Lanfredi, P. S. Saia, R. Lebullenger, and A. C. Hernandes, "Electric conductivity and relaxation in fluoride, fluorophosphate and phosphate glasses: analysis by impedance spectroscopy," *Solid State Ionics*, vol. 146, no. 3-4, pp. 329–339, 2002.

[40] Z. M. Sui, X. Chen, L. Y. Wang et al., "Capping effect of CTAB on positively charged Ag nanoparticles," *Physica E*, vol. 33, no. 2, pp. 308–314, 2006.

[41] L. Francis, A. Balakrishnan, K. P. Sanosh, and E. Marsano, "Hydroxy propyl cellulose capped silver nanoparticles produced by simple dialysis process," *Materials Research Bulletin*, vol. 45, no. 8, pp. 989–992, 2010.

[42] P. Tailhades, B. Gillot, and A. Rousset, "Mixed-valence defect ferrites: a new family of fine powders and thin films of spinel ferrites," *Journal De Physique. IV*, vol. 2, no. 1, p. 249, 1997.

[43] T. Gao, P. Norby, F. Krumeich, H. Okamoto, R. Nesper, and H. Fjellvåg, "Synthesis and properties of layered-structured Mn_5O_8 nanorods," *Journal of Physical Chemistry C*, vol. 114, no. 2, pp. 922–928, 2010.

[44] V. Berbenni and A. Marini, "Oxidation behaviour of mechanically activated Mn_3O_4 by TGA/DSC/XRPD," *Materials Research Bulletin*, vol. 38, no. 14, pp. 1859–1866, 2003.

[45] H. R. Oswald and M. J. Wanpetich, "Die Kristallstrukturen von Mn_5O_8 und $Cd_2Mn_3O_8$," *Helvetica Chimica Acta*, vol. 50, p. 2023, 1967.

[46] S. Fritsch, J. Sarrias, A. Rousset, and G. U. Kulkarni, "Low-temperature oxidation of Mn_3O_4 hausmannite," *Materials Research Bulletin*, vol. 33, no. 8, pp. 1185–1194, 1998.

[47] J. A. Lee, C. E. Newnham, F. S. Stone, and F. L. Tye, "Thermal decomposition of managanese oxyhydroxide," *Journal of Solid State Chemistry*, vol. 31, no. 1, pp. 81–93, 1980.

[48] J. H. Rask and P. R. Buseck, "Topotactic relations among pyrolusite, manganite, and Mn_5O_8: a high-resolution transmission electron microscopy investigation," *American Mineralogist*, vol. 71, no. 5-6, pp. 805–814, 1986.

[49] C. B. Azzoni, M. C. Mozzati, P. Galinetto et al., "Thermal stability and structural transition of metastable Mn_5O_8: in situ micro-Raman study," *Solid State Communications*, vol. 112, no. 7, pp. 375–378, 1999.

[50] E. G. Larson, R. J. Arnott, and D. G. Wickham, "Preparation, semiconduction and low-temperature magnetization of the system $Ni_{1-x}Mn_{2+x}O_4$," *Journal of Physics and Chemistry of Solids*, vol. 23, no. 12, pp. 1771–1781, 1962.

[51] A. M. M. Farea, S. Kumar, K. M. Batoo, A. Yousef, C. G. Lee, and Alimuddin, "Structure and electrical properties of $Co_{0.5}Cd_xFe_{2.5-x}O_4$ ferrites," *Journal of Alloys and Compounds*, vol. 464, no. 1-2, pp. 361–369, 2008.

[52] A. Kumar, B. P. Singh, R. N. P. Choudhary, and A. K. Thakur, "Characterization of electrical properties of Pb-modified $BaSnO_3$ using impedance spectroscopy," *Materials Chemistry and Physics*, vol. 99, no. 1, pp. 150–159, 2006.

[53] K. W. Wagner, "Electricity and magnetism," *Annals of Physics*, vol. 40, p. 817, 1913.

[54] Y. Köseoğlu, M. Bay, M. Tan et al., "Magnetic and dielectric properties of $Mn_{0.2}Ni_{0.8}Fe_2O_4$ nanoparticles synthesized by PEG-assisted hydrothermal method," *Journal of Nanoparticle Research*, vol. 13, no. 5, pp. 2235–2244, 2011.

[55] M. Pastor, S. Goenka, S. Maiti, K. Biswas, and I. Manna, "Phase evolution, dielectric and impedance spectroscopic study of $SrNb_2O_6$ columbite phase," *Ceramics International*, vol. 36, no. 3, pp. 1041–1045, 2010.

[56] T. Ramana, K. Akhilesh, B. Chandrahas, and T. P. Sinha, "Charge transport and dielectric response in ZnO nanotubes," *Current Applied Physics*, vol. 10, p. 676, 2010.

[57] S. F. Mansour and M. A. Elkestawy, "A comparative study of electric properties of nano-structured and bulk Mn-Mg spinel ferrite," *Ceramics International*, vol. 37, no. 4, pp. 1175–1180, 2011.

[58] L. E. Cross, "The contribution of structural disorder to diffuse phase transitions in ferroelectrics," *Ferroelectrics*, vol. 76, p. 241, 1987.

[59] R. Mani, S. N. Achary, K. R. Chakraborty et al., "Dielectric properties of some $MM0_4$ and MTi$M0O_6$ (M01/4 Cr, Fe,Ga; M01/4 Nb, Ta,Sb) rutile-type oxides," *Journal of Solid State Chemistry*, vol. 183, no. 6, pp. 1380–1387, 2010.

[60] J. C. Maxwell, *Electricity and Magnetism*, Oxford University Press, New York, NY, USA, 1973.

[61] Z. Durmus, A. Baykal, H. Kavas, and H. Sozeri, "Preparation and characterization of polyaniline (PANI)-Mn_3O_4 nanocomposite," *Physica B*, vol. 406, p. 1114, 2011.